RESEARCH ARTICLE | NOVEMBER 08 2022

Investigations of process by-products by means of Schlieren imaging during the powder bed fusion of metals using a laser beam

Siegfried Baehr ; Lukas Melzig; Dominik Bauer; Thomas Ammann; Michael F. Zaeh

Check for updates

View Online

Export Citation

11 March 2025 13:06:42

Investigations of process by-products by means of Schlieren imaging during the powder bed fusion of metals using a laser beam

Siegfried Baehr,[1,2,a)] (ID) Lukas Melzig,[1] Dominik Bauer,[2] Thomas Ammann,[2] and Michael F. Zaeh[1]

AFFILIATIONS

[1]Technical University of Munich, TUM School of Engineering and Design, Institute for Machine Tools and Industrial Management, Garching, Bavaria 85748, Germany
[2]Linde GmbH, Carl-von-Linde-Str. 25, Unterschleissheim, Bavaria 85716, Germany

Note: Paper published as part of the special topic on Proceedings of the International Congress of Applications of Lasers & Electro-Optics 2022.
[a)]**Electronic mail:** siegfried.baehr@iwb.tum.de

ABSTRACT

To produce geometrically complex parts with good mechanical properties, various industries increasingly apply the powder bed fusion of metals using a laser beam. Sufficient control of this laser-based additive manufacturing process is necessary to achieve a reliable development as well as reproducible part properties. Besides adjusting the standard process parameters, such as the laser power or the scanning speed, the process gas is an important parameter that influences the part characteristics. In addition to the inertization of the atmosphere, process by-products can be removed during the manufacturing with a constant gas flow across the build plate. Typically, argon or nitrogen is applied. This study investigated the effects of various argon-helium mixtures in comparison to pure argon gas on the heat balance of process by-products during the processing of a high-strength aluminum alloy by means of Schlieren imaging. The method enables visualizations of the process by-products and is further capable of studying evaporation phenomena. For this purpose, a Schlieren imaging setup was designed and installed in an AconityMINI machine. The experimental results were exploited to validate a simplified heat transfer model introduced in this work. The results indicate that the addition of helium to the process gas lowers the amount of fumes and incandescent spatters and thus could decrease evaporation. Also, it was found that the higher thermal conductivity of helium compared to argon leads to significantly higher cooling of process by-products.

I. INTRODUCTION

The powder bed fusion of metals using a laser beam (PBF-LB/M) is an additive manufacturing process, which is gaining increasing relevance in various industries. Its layer-wise build-up procedure overcomes restrictions known from conventional manufacturing and thus offers the possibility of rethinking part designs. Benefits from this freedom of design, such as the functional integration, force-flow optimization or thin-walled structures, along with an adequate mechanical performance of the built parts, make the PBF-LB/M process highly attractive for aerospace, medical, or automotive applications.[1,2]

However, this process still suffers from a comparably low reproducibility and robustness. This is, among other things, due to the high process dynamics.[3] These occur as a result of the high energy input by the laser beam and the high scanning speeds leading to large local heating and cooling rates in the melt pool. As one consequence of that, process by-products appear during manufacturing. These are generally comprised of spatters and vapor. One severe type of spatters is the melt pool ejection originating from a turbulent flow in the melt pool. A vapor plume can additionally emerge if the energy input is sufficiently high to reach the boiling point of volatile alloying elements. The created metal vapor

leads to a recoil pressure resulting in a depression of the melt pool and a higher probability of spattering.[3] Especially in aluminum alloys consisting of alloying elements with low boiling points, such as lithium or magnesium, vaporization can happen.[4] The resulting process instabilities can possibly cause an unstable solidification leading to metallurgical defects. For high-strength aluminum alloys from the 2000 and 7000 series, cracking is a severe type of defects which needs to be avoided. Besides adjustments to the alloy composition to reduce cracking, increasing the process stability by decreasing elemental vaporization can be crucial for a successful fabrication of these alloys.[4]

Various studies numerically and experimentally investigated the governing mechanisms affecting the creation of the process by-products. Their impairing effects on the process,[5,6] on the parts[7–9] and on the powder bed[10–12] were studied. It was shown that the process stability can be negatively influenced through the laser beam attenuation by process by-products. Bidare *et al.* showed that spatters and vapor can interact with the laser beam causing a deflection or a reflection and thus an unsteady energy input.[5] This can lead to part defects, such as lack-of-fusion pores.[6,7] Also, oxidized spatters in the part can lower its surface quality and mechanical performance.[8,9] When a spatter lands on the powder bed and is not being built in the part, it can still cause a decreasing powder quality and a limited recyclability.[10,11] Obeidi *et al.* unveiled that spatters can form non-spherical agglomerates in the powder bed, which increase the degradation of the powder bed.[11] When the powder is reused, these non-spherical spatters, which remained after sieving, can deteriorate the recoating process and finally lead to part defects.[12]

To remove the process by-products and hence to reduce their negative effects on the PBF-LB/M process, a continuous gas flow is applied over the process zone in the PBF-LB/M process.[13] The influence of the gas flow profile and the type of the gas is the subject of current research. Reijonen *et al.* and Ladewig *et al.* highlighted the importance of the gas flow to increase the process capability.[13,14] Further studies indicated that the efficiency of removing process by-products highly depends on the uniformity and velocity of the gas flow.[14,15] The effect of alternative process gas types, other than the standard gases argon (Ar) and nitrogen, showed promising results. It was found that the use of helium (He) containing process gases can lead to less spattering during the processing of AlSi10Mg[16] and Ti-6Al-4V.[17] Pauzon *et al.* attributed this to the lower recoil pressure, which occurs when the lighter He is used instead of Ar.[17] In particular, the creation of less incandescent spatters was observed.[17] This was generally related to the enhanced thermophysical properties of He over Ar. Overall, the use of He showed great potential to reduce the impairing effects of hot spatters on the process and the powder bed. Further studies on Ti-6Al-4V[18,19] and IN718[20] additionally reported positive effects of He on the process and part performance. However, the effect of He as a process gas on the processing of aluminum alloys in the PBF-LB/M process was only poorly studied. The fundamentals of the governing heat transfer phenomena between gas and spatters remain to be described. Within the above-mentioned studies, various process observation techniques, such as high-speed and Schlieren imaging, were successfully applied to study the occurring effects. Especially the application of the Schlieren imaging method

showed promising results in investigating spatters and vapor simultaneously.[3,17] This method utilizes the temperature-dependent refractive index of a transparent medium to highlight different effects linked to the heat balance of the process.[21]

The presented study aims at analytically and experimentally describing the heat transfer between process by-products and He-containing process gases in the PBF-LB/M process. Their influence on the cooling of process by-products is, therefore, investigated analytically using a simplified heat transfer model and experimentally using Schlieren imaging and a thresholding method. The findings from both approaches are then described and discussed. Finally, the experimental results are used to validate the model.

II. HEAT TRANSFER MODEL FOR A SINGLE SPATTER IN THE GAS FLOW

During the PBF-LB/M process, spatters are ejected from the melt pool, travel through the ambient gas atmosphere, and finally settle in the powder bed. During their travel, they experience cooling from the process gas. To gain a basic understanding of the dominating gas properties influencing the cooling of spatters, a heat transfer model was developed. This includes an analytical description of the heat transport phenomena radiation (index "rad") and convection (index "conv"). The resulting total heat flux $\dot{Q}_{total}$ can be expressed as

$$\dot{Q}_{total} = \dot{Q}_{rad} + \dot{Q}_{conv}, \tag{1}$$

with the radiative contribution $\dot{Q}_{rad}$ and the convective contribution $\dot{Q}_{conv}$. Figure 1 shows a schematic representation of the simplified heat transfer model for a single spatter in the gas flow during the PBF-LB/M process. In this study, the index "g" refers to gas properties and the index "s" refers to spatter properties. The following simplifications were made in the heat transfer model:

- The spatters are spherically symmetric.
- A representative relative speed u between the gas flow and the spatter is assumed based on spatter speeds found in the literature.[22]
- The spatter temperature T_s is fixed at a temperature, where aluminum is in the molten state. The gas temperature T_g is set to typical ambient conditions.

With these assumptions, the governing equations for the heat transfer phenomena are described in the following sections.

A. Heat transfer by radiation

The heat transfer by radiation $\dot{Q}_{rad}$ for a nonblackbody radiator is expressed by

$$\dot{Q}_{rad} = \varepsilon_s \cdot \sigma \cdot A_s \cdot T_s^4, \tag{2}$$

with the emission coefficient ε_s, the temperature T_s, and the Stefan–Boltzmann constant $\sigma = 5.67 \times 10^{-8}$ W/(m K^4).[23–25] The spherical spatter surface A_s can be calculated with its diameter
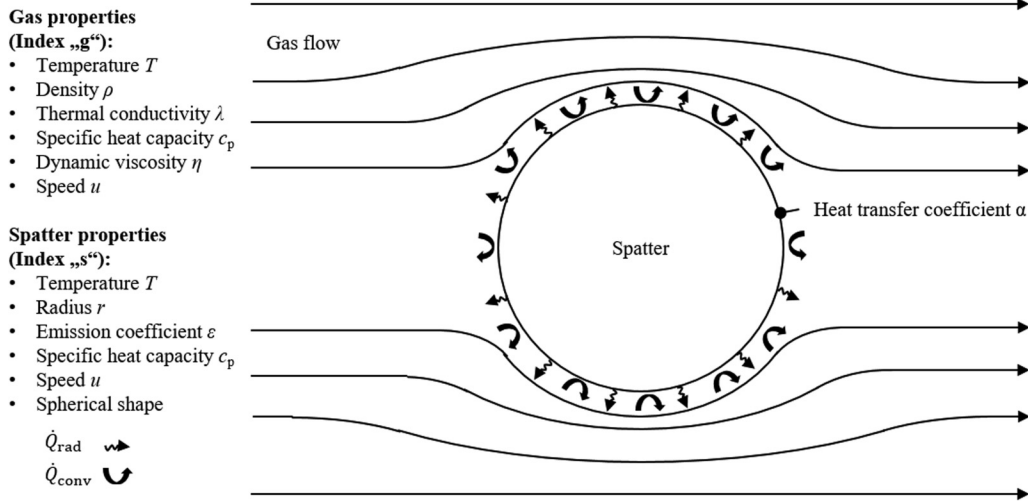
FIG. 1. Schematic representation of a simplified heat transfer model for a single spatter in the gas flow during the PBF-LB/M process; $\dot{Q}_{rad}$ heat flux by radiation, $\dot{Q}_{conv}$: heat flux by convection.

d_s as

$$A_s = d_s^2 \cdot \pi. \tag{3}$$

As it can be seen from Eq. (2), the heat transfer by radiation is purely influenced by the spatter properties and not by the gas properties. However, for the sake of completeness, the radiation is included in the results.

B. Heat transfer by convection

The heat transfer calculation by convection of a spherical particle in a gas flow is a combination of the natural convection (index "nat") and the forced convection (index "forc"). The governing equation for the calculation of the heat flux $\dot{Q}_{conv}$ is

$$\dot{Q}_{conv} = \alpha \cdot A_s \cdot \Delta T, \tag{4}$$

with

$$\Delta T = T_s - T_g, \tag{5}$$

expressing the temperature difference between the spatter and the gas.[23] The heat transfer coefficient α is derived from the dimensionless Nusselt number Nu_{conv},

$$Nu_{conv} = \frac{\alpha \cdot d_s}{\lambda_g}. \tag{6}$$

To account for both convection phenomena, Nu_{conv} is calculated by $Nu_{conv,nat}$ for the natural convection and $Nu_{conv,forc}$ for the forced convection via the equation for the mixed convection by the authors of Ref. 24 according to

$$Nu_{conv} = \sqrt[3]{Nu_{conv,nat}^3 + Nu_{conv,forc}^3}. \tag{7}$$

Equation (7) is valid for a range of the dimensionless Prandtl numbers Pr with $0.1 < Pr < 100$.[26] The empirical correlation for $Nu_{conv,nat}$ for a spherical particle is formulated using

$$Nu_{conv,nat} = 0.56 \cdot \left[\left(\frac{Pr}{0.846 + Pr} \right) \cdot Ra \right]^{\frac{1}{4}} + 2, \tag{8}$$

with the dimensionless Rayleigh number Ra according to Ref. 27. For the calculation of $Nu_{conv,forc}$, a laminar and a turbulent flow regime need to be considered according to

$$Nu_{conv,forc} = 2 + \sqrt{Nu_{lam,forc}^2 + Nu_{turb,forc}^2}, \tag{9}$$

as the heat transfer is highly influenced by the flow regime.[28] The laminar (index "lam") $Nu_{lam,forc}$ and the turbulent (index "turb") $Nu_{turb,forc}$ are described by

$$Nu_{lam,forc} = 0.664 \cdot \sqrt{Re} \cdot \sqrt{Pr}, \tag{10}$$

and

$$Nu_{turb,forc} = \frac{0.037 \cdot Re^{0.8} \cdot Pr}{1 + 2.443 \cdot Re^{-0.1} \cdot (Pr^{2/3} - 1)}, \tag{11}$$

with the dimensionless Reynolds number Re according to.[28] Pr, Ra, and Re are material and gas-specific entities and calculated by

$$Pr = \frac{v_g}{a_g}, \tag{12}$$

$$Ra = \frac{\beta_g \cdot g \cdot \Delta T \cdot d_s^3}{v_g \cdot a_g} \text{ and} \tag{13}$$

TABLE I. Relevant physical properties of the used process gases argon (Ar) and helium (He) as well as two ar-He mixtures: ρ_g: density, λ_g: thermal conductivity, $c_{p,g}$: specific heat capacity, η_g: dynamic viscosity.

	Ar	70 vol. % Ar + 30 vol. % He	30 vol. % Ar + 70 vol. % He	He
ρ_g (kg/m^3)	1.612	1.177	0.597	0.162
λ_g [W/(m K)]	0.0177	0.0390	0.0870	0.1536
$c_{p,g}$ [J/(kg K)]	520	712	1405	5193
η_g (Pa s)	22.6×10^{-6}	23.2×10^{-6}	23.6×10^{-6}	19.8×10^{-6}

$$Re = \frac{d_s \cdot u}{v_g}, \tag{14}$$

with the thermal expansion coefficient β_g and the gravitational acceleration g according to Ref. 23. The temperature conductivity a_g and the kinematic viscosity v_g can be derived from gas-specific entities by

$$a_g = \frac{\lambda_g}{\rho_g \cdot c_{p,g}} \text{ and} \tag{15}$$

$$v_g = \frac{\eta_g}{\rho_g}, \tag{16}$$

with the thermal conductivity λ_g, the density ρ_g, the specific heat capacity c_p, and the dynamic viscosity η_g. The presented equations for the calculation of the heat transfer by convection $\dot{Q}_{conv}$ are valid when $10^{-1} < Re < 10^4$ and $0.6 < Pr < 10\,000$ hold. As Pr results in values outside these limits for the Ar-He gas mixtures, a linear correlation for the calculation of $\dot{Q}_{conv}$ was used instead for these gases due to a lack of a more suitable model.

C. Cooling time

The cooling time t of a spatter can be calculated from the total heat flux $\dot{Q}_{total}$ via its specific heat,[23]

$$\dot{Q}_{total} \cdot t = c_{p,s} \cdot m_s \cdot \Delta T. \tag{17}$$

The mass of a single spherical spatter m_s can be derived from its density ρ_s and its volume V_s,

$$m_s = \rho_s \cdot V_s = \frac{\rho_s \cdot \pi \cdot d_s^3}{6}. \tag{18}$$

TABLE II. Generic gas (index "g") and spatter (index "s") properties used in this work.

Parameter	Value
Spatter diameter, d_s	100×10^{-6} m^3
Thermal expansion coefficient, β_g	0.003 354 1/K
Temperature gas, T_g	298.15 K
Temperature spatter, T_s	1273.15 K
Emission coefficient, ε_s	0.4
Relative speed $u = |u_g - u_s|$ between the gas and a spatter	10 m/s

For the calculations, the parameters given in Tables I and II were used.[29]

III. MATERIALS AND METHODS

A. Experimental procedure

The experiments were carried out on a research scale PBF-LB/M machine (AconityMINI, Aconity3D, Germany). This machine was equipped with a 500 W laser with a wavelength of 1064 nm and a laser spot size of 80 μm. The powder material used in the experiments was a gas-atomized high-strength aluminum alloy AA2195 pre-alloyed with 1.8 m% zirconium (Nanoval, Germany). The density of the alloy ρ_s was given with 2680 kg/m^3. The particle size distribution of the alloy ranged from 21 to 66 μm. The chemical composition of the alloy, which was given by the manufacturer, is shown in Table III.

The build job layout consisted of a single scan vector with a length of 10 mm, oriented as shown in Fig. 2. The laser power and the scanning speed were set to 300 W and 1000 mm/s, respectively. Throughout this study, the y-direction refers to the scanning direction and the z-direction refers to the building direction. Four process gases were considered in this study: Ar, 70 vol. % Ar + 30 vol. % He, 30 vol. % Ar + 70 vol. % He and He. The experiments were conducted in a pure gas atmosphere without a gas flow and in a single execution.

B. Schlieren imaging

1. Principle of schlieren imaging

When light interacts with matter, it is slowed down. The refractive index n_g of a transparent medium can be calculated by

$$n_g = \frac{c_0}{c}, \tag{19}$$

with the speed of the propagation of light within the medium c and the speed of light in vacuum c_0.[21] The refractive index of gases

TABLE III. Chemical composition of the zirconium pre-alloyed aluminum alloy AA2195.

Element	Al	Cu	Li	Mg	Ag	Zr
m%	Rest	4.0	1.0	0.5	0.4	1.8
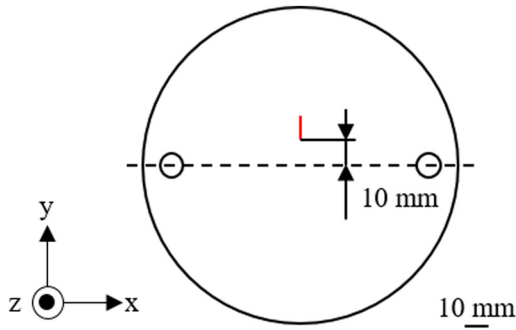
FIG. 2. Build job layout (the vertically centered single scan vector is indicated by a red line); y: scanning direction, z: building direction.

linearly relates to the gas density ρ_g according to

$$n_g - 1 = k \cdot \rho_g. \tag{20}$$

The Gladstone–Dale coefficient k has a value of 0.23 cm³/g for air at standard conditions and varies from 0.1 to 1.5 cm³/g for other gases. The refractive index is only slightly dependent on the gas density ρ_g. A variation of ρ_g of two orders of magnitude results only in a 3% change of n_g. In addition to the density, the gas composition and the wavelength of the illumination can generally influence the refractivity ($n-1$) of a gas.[21]

Using the ideal gas state equation at or near atmospheric conditions,

$$\frac{p_g}{\rho_g} = R \cdot T_g, \tag{21}$$

with the specific gas constant R and the density of the gas ρ_g, n_g can be related to the pressure p_g and temperature T_g of the gas. Pressure and temperature fluctuations lead to changes in the gas density, to a change in the refractive index and thus to the deflection of light rays, which visualize irregularities within the gas. This shall be illustrated according to the coordinate system in Fig. 2: If the y-direction is the direction in which the light propagates, single beams of light might be affected by regions of optical irregularity. It can be shown that these optical inhomogeneities deflect or refract light according to their gradient of the refractive index in the x-z-plane perpendicular to its direction of propagation. The resulting deflections can be formulated by

$$\frac{\partial^2 x}{\partial y^2} = \frac{1}{n} \cdot \frac{\partial n}{\partial x} \quad \text{and} \tag{22}$$

$$\frac{\partial^2 z}{\partial y^2} = \frac{1}{n} \cdot \frac{\partial n}{\partial z}, \tag{23}$$

with the three coordinates x, y, and z.[21] When considering a two-dimensional Schlieren imaging with the propagation of light over a distance L along the y-direction, the angular deflection ε in the

x- and in the z-direction can be described after a single integration of Eqs. (22) and (23) by

$$\varepsilon_x = \frac{L}{n_g} \cdot \frac{\partial n}{\partial x} \quad \text{and} \tag{24}$$

$$\varepsilon_z = \frac{L}{n_g} \cdot \frac{\partial n}{\partial z}, \tag{25}$$

with n_g as the refractive index of the surrounding medium.[21] The gradients in the x- and z-direction are responsible for the refraction of light, but do not influence the value of the refractive index n. Equations (24) and (25) show that light is always deflected toward the area of a higher n. For gases, according to Eq. (20), this means that refraction occurs in the direction of the region of a higher density ρ_g. This phenomenon of inhomogeneous transparent media is called Schlieren and manifests itself as relatively small differences in refractivity relative to the background. It causes refraction in all directions except the undisturbed direction of light propagation. Schlieren can have a gradient of the refractive index in one, two, or three spatial directions.

2. Custom schlieren imaging

In the present study, a custom Schlieren imaging setup was designed and integrated into the PBF-LB/M machine (see Fig. 3). It was designed as a Toepler's lens-type Schlieren imaging setup.[21] In the following description, the designations in brackets prior to the component refer to Fig. 3. Light from an (a) LED (MCWHL6, Thorlabs, Germany) with a wavelength between 400 and 800 nm was guided through a (b) plano-convex lens (LA1417-A-ML, Thorlabs, Germany) with a diameter of 25 mm and a focal length of 150 mm to establish a (c) collimated light beam. The collimated light beam was then deflected by a (d) deflection mirror (CCM1-G01/M, Thorlabs, Germany) by 90° into the x-z-plane to travel over the build plate of the PBF-LB/M machine. The build plate represented the (e) test area where phenomena that occurred during the process under the influence of various process gases could be investigated. The light beam was then guided through a (f) second and third deflecting mirror to leave the build chamber towards the (g) second plano-convex lens with a diameter of 25 mm and a focal length of 150 mm. The second plano-convex lens focused each of the light beams deflected by the Schlieren object in the test area onto a corresponding point on the optical screen or in a camera. When an (h) optical slit (cut-off) is placed in the focal point of the (g) lens and closed to a certain extent, rays of light might be blocked depending on their deflection. The point on the screen corresponding to this blocked ray appears dark. In this point of the inhomogeneity within the test area, the phase difference that creates a vertical gradient $\delta n/\delta z$ in the test area induces a difference in amplitude, resulting in the previously invisible Schlieren object being made visible. In the actual process, many light rays are deflected by this in many directions. All rays deflected and therefore potentially blocked by the cut-off partially image the Schlieren object as a shadow on a bright background on the screen. The slit in this study could be adjusted in both the horizontal and
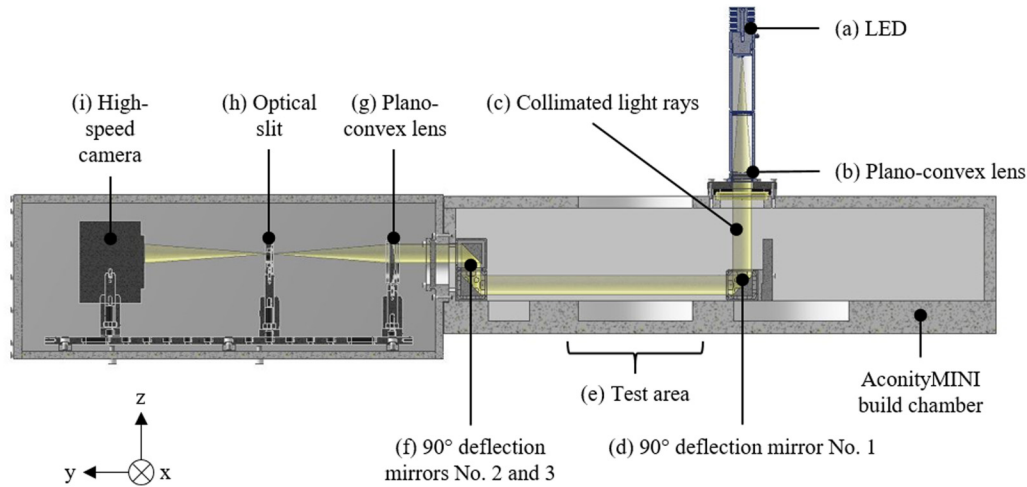
FIG. 3. Custom Schlieren imaging setup; LED: light emitting diode.

vertical direction and was closed in both directions to such an extent that most of the focused light beam was blocked by it. In this way, a high contrast and sharp Schlieren image could be recorded by the (i) high-speed camera (i-Speed 3, Olympus, Germany) behind it. The frame rate of the high-speed camera was selected to achieve the highest possible image resolution. Thus, the camera recorded a monochrome video with a frame rate of 2000 fps at a resolution of 1280×1024 pixels. A real-time image of the custom Schlieren imaging setup can be found in Fig. A1 in the Appendix.[32]

3. Schlieren video analysis by means of thresholding

Besides qualitatively analyzing the gathered high-speed Schlieren videos, they were post-processed by means of thresholding. Therefore, the software systems IMAGEJ (version: 1.53r) and MATLAB (version: R2021b) were utilized. In a Schlieren video, hot spatters are assumed to glow brighter (incandescent spatter) than cold spatters. To highlight areas with various brightness levels, a stepwise thresholding approach was applied (see Fig. 4). Initially,

the threshold was set to the maximum black (255/0), which means that the entire image appeared black. The threshold value for black was then reduced in ten steps, from 255/0 to 80/0, whereby the brightly glowing spatters became visible step by step. The brightest and, therefore, hottest spatters appeared first. An image (for all gases at the same point in time) was stored for each threshold level. In these images, hot spatters were represented by white pixels, while the rest was filled with black pixels. When these images for the individual threshold levels were converted into matrices, white pixels were assigned the value 1 and black pixels the value 0. Adding up these matrices finally resulted in a value indicating how often a pixel was assigned a value of 1 and is, therefore, part of the appearance of a hot spatter. In a further step, three frequency levels for the number of appearances of a hot spatter were defined, which had a color gradient from red to blue with decreasing frequency. When the red area farthest from the melt pool was identified for each of the used process gases, the maximum distance that a hot spatter could travel before being cooled to a lower level could be determined. When a radial heat and momentum transfer of process by-products is assumed,

<div align="right">11 March 2025 13:06:42</div>
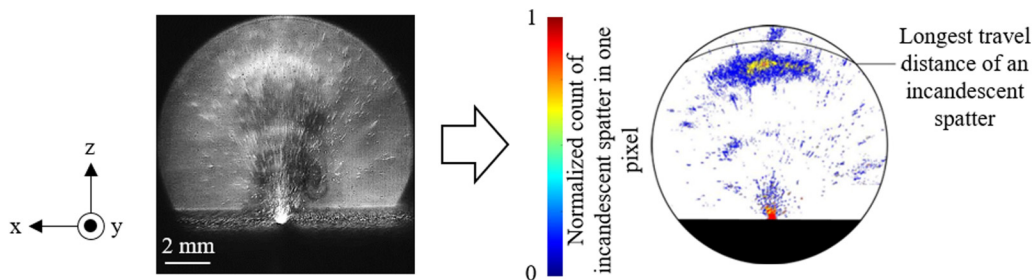
FIG. 4. Thresholding method to track incandescent spatter.

following the literature,[5] a circular line could be drawn through the farthest point with its distance to the melt pool as the radius. Hence, this procedure allowed assumptions about the cooling rate of the spatters under various process gases.

IV. RESULTS AND DISCUSSION

A. Heat transfer model

To enhance the comparability between the gases, the calculated heat fluxes by the analytical model were normalized based on the heat flux achieved in a reference condition. For the latter, the process with Ar was chosen as the reference in the course of this study. The normalized heat fluxes $\bar{Q}$ were calculated by

$$\bar{Q} = \frac{\dot{Q}}{\dot{Q}_{Ar}} \; . \tag{26}$$

The results of the calculations of the heat balance are shown in Fig. 5.

As it can be seen, the heat transfer increases with an increasing volume fraction of He in Ar. Also, the main influence of the heat transfer by convection compared to radiation is unveiled. This was also shown in literature, where the comparably low contribution of the radiation as a consequence of the Stefan–Boltzmann constant was highlighted.[6] Considering the total heat transfer, the cooling ability of He was found to be about 4.6 times as high as that of Ar. This might be related to the higher thermophysical properties of He compared to Ar (see Table I). These findings
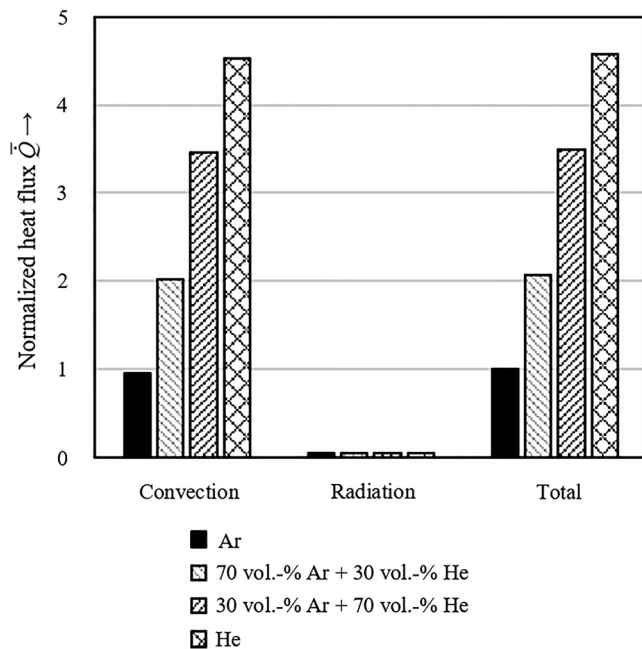
confirm the experimental results found in literature, where various mechanical test specimens from Ti-6Al-4V[18,19] and IN718[20] showed greater performance when produced under He-containing atmosphere compared to Ar, which was attributed to the enhanced cooling ability of He. In the calculation of the heat transfer by convection, the increased thermophysical properties of He led to higher Pr and Ra numbers and thus to a higher heat transfer by convection [see Eqs. (4)–(13)]. When investigating the influencing factors on the heat transfer by convection based on the developed heat transfer model individually, it became evident that an increasing λ_g shows a dominating influence rather than an increasing $c_{p,g}$ (see Fig. 6).

As shown in the figure, a difference in the specific heat capacity $c_{p,g}$ of a factor of about ten, as it is the case between Ar and He, only leads to a minor change in the overall heat transfer. On the opposite, an increase in the thermal conductivity λ_g of a factor of about nine leads to a significant increase in the overall heat transfer. When transferring these findings to the PBF-LB/M process, this means that both gases offer a comparable thermal mass. It is the higher thermal conductivity λ_g of He in comparison to Ar, which leads to the enhanced cooling of process by-products.

B. Schlieren imaging

Figure 7 schematically shows the results for the thresholding approach to determine the farthest distance that a hot spatter traveled before being cooled down.

The maximum travel distance of a hot spatter varied depending on the applied process gas (see Fig. 7). The farthest distance

FIG. 5. Normalized heat flux $\bar{Q}$ by different heat transfer phenomena for different process gases as a result of the developed model (reference: Ar).
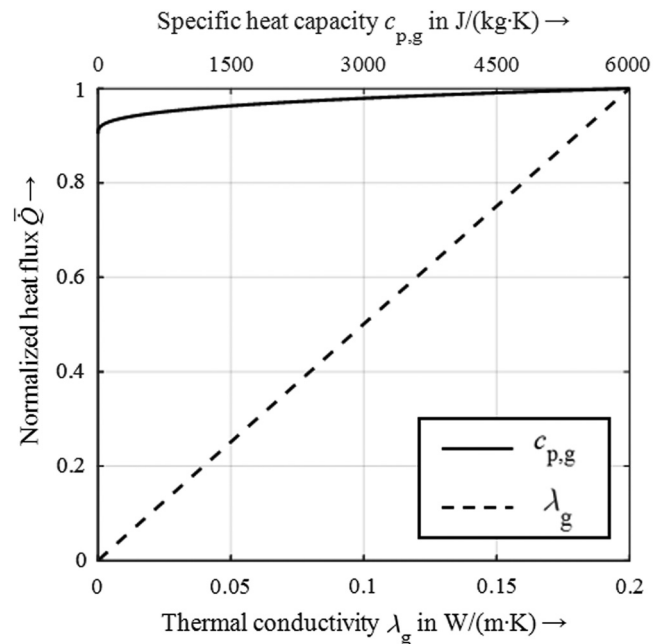
FIG. 6. Influence of the thermal conductivity λ_g and the specific heat capacity $c_{p,g}$ on the normalized heat flux calculated with the developed model.
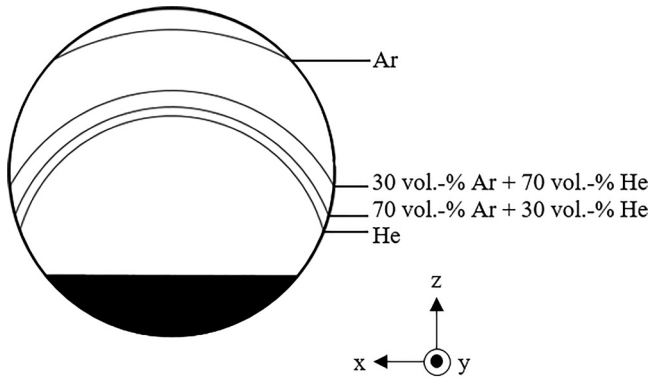
FIG. 7. Schematic result of the thresholding approach to determine the furthest travel distance of a high normalized count of incandescent spatter.

was detected for Ar, the shortest distance for He. These results generally matched with the findings from the heat transfer model, where a higher cooling effect was shown for He in comparison to Ar. This trend was not found for the Ar-He mixtures, where 70 vol. % Ar + 30 vol. % He showed a slightly shorter distance than 30 vol. % Ar + 70 vol. % He. This, if not due to an experimental error, indicates that the assumption of a linear correlation for the heat flux calculations was not suitable for those gases. However, this aspect remains undiscussed within this paper and needs to be investigated in the future.

When the Schlieren imaging results for the various gases were additionally analyzed qualitatively, the differences in the heat transfer were confirmed. Figure 8, therefore, shows the final images of the respective process videos. With an increasing fraction of He in Ar and thus a decreasing density ρ_g from Figs. 8(a) to 8(d), it was observed that spatters could expand in a wider angle into the atmosphere. This was also reported in the literature, where a faster expansion of spatters was found in He-containing atmospheres and attributed to its comparably lower molecular mass.[17,30] However, these spatters were found to be remolten by the laser beam and

thus not to be incorporated in the total amount of spatters.[30] Considering the glowing of the particles as an indicator for their temperature, less incandescent spatters were found in the He-containing processes. This was also confirmed by the visible differences in the refractive index gradients around the spatters, which resulted in more pronounced Schlieren in Ar than in He. Results from previous studies corroborate these findings.[17] Besides the spatters, a vapor plume could be identified over the process zone in the Schlieren image of the Ar process compared to the He-containing process [see Fig. 8(a)]. As described in the principles of Schlieren imaging, the angular deflection of light ε and thus the strength of a single Schliere in the final image depends on the refractive index n_g [Eqs. (24) and (25)]. The refractive index n_g is in a linear relation with the gas density [see Eq. (20)], which itself depends on the temperature [Eq. (21)]. For a similar set of process parameters, a certain amount of melt evaporates and creates a vapor plume above the process zone. This hot vapor plume is rapidly cooled off in the ambient atmosphere. Differences in the vapor plume temperature would thus result in lower gradients in the refractive index. This was found in the He-containing processes, where no or only a weak vapor plume occurred [see Figs. 8(b) and 8(c)]. This result of lower gradients in the refractive index for He was also described in a previous study on 316L stainless steel.[5] The rapid cooling of the plume led to the formation of a metal condensate, which consisted of solid particles appearing as black dots in the Schlieren image. With the higher cooling ability of He, besides spatters, primarily condensate particles were visible in the He-containing Schlieren images. On the opposite, a clear vapor plume was only apparent in the Ar Schlieren image. This absence of a vapor plume could lead to less laser attenuation in the PBF-LB/M process and hence to a more stable process in He-containing atmospheres.

C. Experimental model validation

In the heat balance model, a ratio $\dot{Q}_{total,He}/\dot{Q}_{total,Ar} = 4.57$ was found between He and Ar regarding their cooling abilities (see Fig. 5). To validate this with the experimental results, a ratio for the cooling time t between Ar and He was derived by the Schlieren images. As
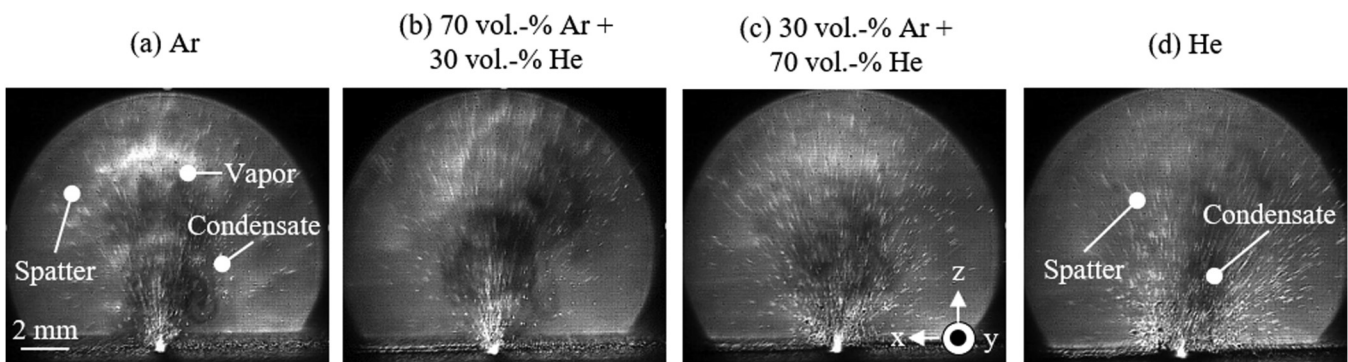
FIG. 8. Schlieren images for various process gases.

11 March 2025 13:06:42
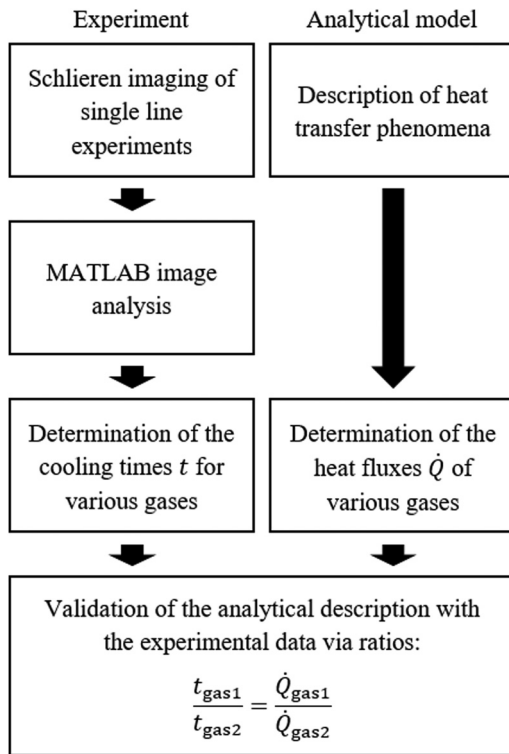
FIG. 9. Flow chart describing the validation approach for the heat transfer model.

described in previous sections, the glowing of a spatter in the Schlieren videos could be used as an indicator for its cooling. Thus, the number of frames from a spatter leaving the melt pool until it is visibly cooled down was determined utilizing the thresholding method. This number translated to the cooling time t via the given frame rate of the high-speed camera. When assuming a similar temperature difference ΔT within this time, t and the heat fluxes $\dot{Q}_{total}$ from the model could be used for validation [Eqs. (17) and (18)]. Due to a lack of data for the used alloy, $c_{p,s}$ was taken for pure aluminum in the molten state at 973.15 K and set to 1100 J/(kg K) for the calculations.[31] This validation approach is summarized and visualized in Fig. 9. The results of the approach are given in Table IV.

As it can be seen in the table, the presented validation approach led to a ratio t_{Ar}/t_{He} of 4.67. This ratio described how

TABLE IV. Experimentally determined cooling times t and temperature differences ΔT.

	Ar	He
No. of frames until spatters cooled off	14	3
t (s)	0.007	0.0015
Experimental cooling ratio (t_{Ar}/t_{He})	4.67	
ΔT (K)	354.70	347.40

much more time was required in Ar for a spatter to stop glowing compared to He. It could therefore be compared to the above-mentioned ratio $\dot{Q}_{total,He}/\dot{Q}_{total,Ar} = 4.57$ from the heat transfer model, which described the higher cooling ability of He compared to Ar. Also, ΔT for both gases was found to be comparable, which therefore fulfills the basic assumption for these calculations.

However, this validation approach was subject to estimations. First, the exact specific heat capacity of the liquid was unknown. Also, a loss of information between two frames was inevitable within the given experimental setup. The cooling time t calculated from the number of frames, therefore, did not necessarily need to indicate the real cooling behavior, as the spatter could already be cooled off in between two frames. This was not considered in the presented validation. However, taking these limitations into account, the simplified model can generally describe the occurring heat transfer phenomena between a single spatter and the process gas in PBF-LB/M.

V. CONCLUSIONS

During the PBF-LB/M process, by-products, such as spatters and vapor, occur. These by-products can decrease the process capability. A possible solution to reduce their impairing effects on the process is the use of He or He-containing process gases, leading to a faster cooling of the process by-products. To study the occurring effects, a simplified heat transfer model was set up in this work. The model included convective and radiative heat transfer and thus enabled the comparison of various process gases regarding their cooling ability. The four process gases Ar, He, 70 vol. % Ar + 30 vol. % He and 30 vol. % Ar + 70 vol. % He were compared in this study. Besides the analytical investigations, a custom Schlieren imaging setup was built up and utilized to experimentally investigate and confirm the findings of the heat transfer model. Finally, the experimental results were used to validate the model.

In summary, the following conclusions regarding the PBF-LB/M process were derived from this study:

- The cooling of process by-products increases with a rising fraction of He in the process gas (up to a factor of ≈ 4.6 for He compared to Ar).
- The removal of heat during the cooling of process by-products is dominated by the thermal conductivity λ_g rather than by the specific heat capacity $c_{p,g}$ of the process gas.
- A reduced vapor plume and fewer incandescent spatter appear when using He-containing process gases compared to Ar.
- The enhanced cooling ability of He-containing process gases is a material-independent effect.

In future works, experimental investigations on the chemical composition of the powder and the solidified bulk material must be carried out. This enables the identification of the alloy evaporation intensity with the use of He. Therefore, the influence of He-containing process gases on the cooling of the melt pool will be of particular interest.

11 March 2025 13:06:42

AUTHOR DECLARATIONS

Conflict of Interest

The authors have no conflicts to disclose.

Author Contributions

Siegfried Baehr: Conceptualization (lead); Formal analysis (lead); Investigation (lead); Methodology (lead); Validation (lead); Visualization (lead); Writing – original draft (lead). **Lukas Melzig:** Investigation (supporting). **Dominik Bauer:** Investigation (supporting); Methodology (supporting). **Thomas Ammann:** Project administration (equal); Supervision (equal). **Michael F. Zaeh:** Project administration (equal); Supervision (equal).

REFERENCES

[1]G. Rasiya, A. Shukla, and K. Saran, "Additive manufacturing—A review," Mater. Today: Proc. **47**, 6896–6901 (2021).

[2]A. Vafadar, F. Guzzomi, A. Rassau, and K. Hayward, "Advances in metal additive manufacturing: A review of common processes, industrial applications, and current challenges," Appl. Sci. **11**, 1213–1242 (2021).

[3]Z. A. Young, Q. Guo, N. D. Parab, C. Zhao, M. Qu, L. I. Escano, K. Fezzaa, W. Everhart, T. Sun, and L. Chen, "Types of spatter and their features and formation mechanisms in laser powder bed fusion additive manufacturing process," Addit. Manuf. **36**, 101438 (2020).

[4]J. Zhang, B. Song, Q. Wei, D. Bourell, and Y. Shi, "A review of selective laser melting of aluminum alloys: Processing, microstructure, property and developing trends," J. Mater. Sci. Technol. **35**, 270–284 (2019).

[5]P. Bidare, I. Bitharas, R. M. Ward, M. M. Attallah, and A. J. Moore, "Fluid and particle dynamics in laser powder bed fusion," Acta Mater. **142**, 107–120 (2018).

[6]S. A. Kairallah, A. T. Anderson, A. Rubenchik, and W. E. King, "Laser powder-bed fusion additive manufacturing: Physics of complex melt flow and formation mechanisms of pores, spatter, and denudation zones," Acta Mater. **108**, 36–45 (2016).

[7]J. Liu and P. Wen, "Metal vaporization and its influence during laser powder bed fusion process," Mater. Des. **215**, 110505 (2022).

[8]D. Wang, S. Wu, F. Fu, S. Mai, Y. Yang, Y. Liu, and C. Song, "Mechanisms and characteristics of spatter generation in SLM processing and its effect on the properties," Mater. Des. **117**, 121–130 (2017).

[9]M. T. Andani, R. Dehghani, M. R. Karamooz-Ravari, R. Mirzaeifar, and J. Ni, "Spatter formation in selective laser melting process using multi-laser technology," Mater. Des. **131**, 460–469 (2017).

[10]M. Lutter-Günther, M. Bröker, T. Mayer, S. Lizak, C. Seidel, and G. Reinhart, "Spatter formation during laser beam melting of AlSi10Mg and effects of powder quality," Procedia CIRP **74**, 33–38 (2018).

[11]M. A. Obeidi, A. Mussatto, R. Groarke, R. K. Vijayaraghavan, A. Conway, F. R. Kaschel, E. McCarthy, O. Clarkin, R. O'Connor, and D. Brabazon, "Comprehensive assessment of spatter material generated during selective laser melting of stainless steel," Mater. Today Commun. **25**, 101294 (2020).

[12]L. Haferkamp, L. Haudenschild, A. Spierings, K. Wegener, K. Riener, S. Ziegelmeier, and G. J. Leichtfried, "The influence of particle shape, powder flowability, and powder layer density on part density in laser powder Bed fusion," Metals **11**, 418–431 (2021).

[13]J. Reijonen, A. Revuelta, T. Riipinen, K. Ruusuvuori, and P. Puukko, "On the effect of shielding gas flow on porosity and melt pool geometry in laser powder bed fusion additive manufacturing," Addit. Manuf. **32**, 101030 (2020).

[14]A. Ladewig, G. Schlick, M. Fisser, V. Schulze, and U. Glatzel, "Influence of the shielding gas flow on the removal of process by-products in the selective laser melting process," Addit. Manuf. **10**, 1–9 (2016).

[15]B. Ferrar, L. Mullen, E. Jones, R. Stamp, and C. J. Sutcliffe, "Gas flow effects on selective laser melting (SLM) manufacturing performance," J. Mater. Process. Technol. **212**, 355–364 (2012).

[16]A. Wimmer, C. Zeller, F. Bayerlein, D. Scherer, M. F. Zaeh, P. Forêt, and J. Scholz, "Influence of the Process Gas on the Laser Beam Melting Process," *Proceedings of 7th International Conference on Additive Technologies October 2018*, Maribor, Slovenia (Interesansa - zavod, Ljubljana, 2018), pp. 66–70.

[17]C. Pauzon, B. Hoppe, T. Pichler, S. Dubiez-Le Goff, P. Forêt, T. Nguyen, and E. Hryha, "Reduction of incandescent spatter with helium addition to the process gas during laser powder bed fusion of Ti-6Al-4V," CIRP J. Manuf. Sci. Technol. **35**, 371–378 (2021).

[18]C. Pauzon, P. Forêt, E. Hryha, T. Arunprasad, and L. Nyborg, "Argon-Helium mixtures as laser-powder Bed fusion atmospheres: Towards increased build rate of Ti-6Al-4V," J. Mater. Process. Technol. **279**, 116555 (2020).

[19]H. Amano, T. Ishimoto, R. Suganuma, K. Aiba, S.-H. Sun, R. Ozasa, and T. Nakano, "Effect of a helium gas atmosphere on the mechanical properties of Ti-6Al-4V alloy built with laser powder bed fusion: A comparative study with argon gas," Addit. Manuf. **48**, 102444 (2021).

[20]C. Pauzon, T. Mishurova, M. Fischer, J. Ahlström, T. Fritsch, G. Bruno, and E. Hryha, "Impact of contour scanning and helium-rich process gas on performances of alloy 718 lattices produced by laser powder bed fusion," Mater. Des. **215**, 110501 (2022).

[21]G. S. Settles, *Schlieren and Shadowgraph Techniques: Visualizing Phenomena in Transparent Media* (Springer, Berlin, Heidelberg, 2001), p. 394.

[22]C. Barrett, C. Carradero, E. Harris, K. Rogers, E. MacDonald, and B. Conner, "Statistical analysis of spatter velocity with high-speed stereovision in laser powder bed fusion," Prog. Addit. Manuf. **4**, 423–430 (2019).

[23]H. D. Baehr and K. Stephan, *Heat and Mass Transfer* (Springer, Berlin, Heidelberg, 2011), p. 758.

[24]The NIST Reference on Constants, Units, and Uncertainty, National Institute of Standards and Technology.

[25]S. W. Churchill, "A comprehensive correlating equation for laminar, assisting, forced and free convection," AIChE J. **23**, 10–16 (1977).

[26]B. F. Armaly, T. S. Chen, and N. Ramachandran, "Correlations for laminar mixed convection on vertical, inclined and horizontal flat plates with uniform surface heat flux," Int. J. Heat Mass Transfer **30**, 405–408 (1987).

[27]G. D. Raithby and K. G. T. Hollands, "A general method of obtaining approximate solutions to laminar and turbulent free convection problems," Adv. Heat Transfer **11**, 265–315 (1975).

[28]M. Kraume, *Transportvorgänge in der Verfahrenstechnik* (Springer, Berlin, Heidelberg, 2004), p. 613.

[29]Linde GmbH, (2022) Internal Database of Gas Properties.

[30]M. A. Stokes, S. A. Khairallah, A. N. Volkov, and A. M. Rubenchik, "Fundamental physics effects of background gas species and pressure on vapor plume structure and spatter entrainment in laser melting," Addit. Manuf. **55**, 102819 (2022).

[31]D. Dragulin and M. Ruther, "Specific heat capacity of aluminium and aluminium alloys," Heat Treat. **3**, 81–85 (2018).

[32]See supplementary material at https://www.scitation.org/doi/suppl/10.2351/7.0000808 for contains a real-time image of the custom Schlieren imaging setup.